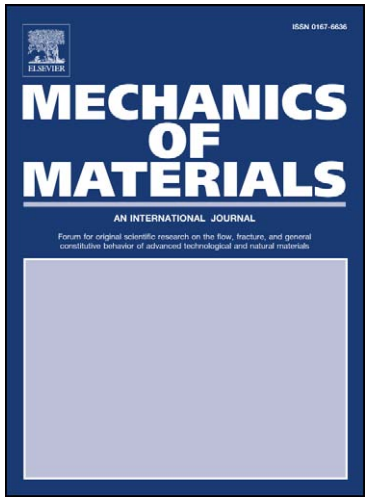

Study of the yielding of sand under generalized stress conditions using a versatile hollow cylinder torsional apparatus

Brendan C. O'Kelly, Patrick J. Naughton

PII: S0167-6636(08)00155-5
DOI: 10.1016/j.mechmat.2008.11.002
Reference: MECMAT 1644

To appear in: *Mechanics of Materials*

Received Date: 15 June 2007
Revised Date: 8 October 2008
Accepted Date: 11 November 2008

Please cite this article as: O'Kelly, B.C., Naughton, P.J., Study of the yielding of sand under generalized stress conditions using a versatile hollow cylinder torsional apparatus, *Mechanics of Materials* (2008), doi: 10.1016/j.mechmat.2008.11.002

Study of the yielding of sand under generalized stress conditions using a versatile hollow cylinder torsional apparatus

Brendan C. O'Kelly (corresponding author)

Lecturer,

Department of Civil, Structural and Environmental Engineering,

Museum Building, Trinity College Dublin, Dublin 2, Ireland.

Tel. +353 18962387 Fax. +353 16773072 E-mail: bokelly@tcd.ie

Patrick J. Naughton

Lecturer in Civil Engineering,

School of Engineering,

Institute of Technology, Sligo,

Ballinode, Sligo, Ireland.

Tel. +353 719155489 Fax. + 353 719155390 E-mail: naughton.patrick@itsligo.ie

First submission: 15th June 2007

Resubmitted: 8th October 2008

Abstract

The hollow cylinder torsional apparatus (HCTA) is particularly suited to studying the mechanical behavior of cross-anisotropic test specimens since the magnitudes of the three principal stresses and the orientation of the major-minor principal stress axes can be independently controlled. Novel features of the University College Dublin HCTA, particularly the instrumentation and calibration procedures necessary to achieve accurate generalized stress path testing, are presented. The plastic yield behavior of fully saturated Leighton Buzzard sand was studied under generalized stress conditions. Physically identical test-specimens (35.5 mm inner radius, 50.0 mm outer radius and 200 mm in length) were prepared using a water-pluviation technique that reproduces the inherent cross-anisotropic fabric of many natural sand deposits. A series of stress path tests systematically probed the stress space to locate segments of yield loci. The deviator stress at yield was found to vary in a well-defined pattern that depended on the magnitude of the intermediate principal stress parameter. However, the deviator stress at yield was largely independent of reorientations of the major principal stress that had occurred during the initial anisotropic consolidation stage of the tests. The experimental yield data was used to show that the Matsuoka-Nakai and Lade yield criteria provide satisfactory predictions of the onset of plastic yielding in sand deposits under generalized stress conditions for routine geotechnical engineering design.

Keywords: Hollow cylinder apparatus; Torsion; Sand; Stress path; Yield; Yield criterion

Nomenclature

b	intermediate principal stress parameter
H	specimen length
HCTA	hollow cylinder torsional apparatus
J_1, J_2 and J_3	first, second and third effective stress invariants
p	mean confining stress
p’	mean effective confining stress
p_i and p_e	inner and outer confining pressures, respectively
r_i and r_e	inner and outer specimen radii, respectively
R	major-to-minor principal stress ratio
R’	major-to-minor effective principal stress ratio
T	torque
q	deviator stress
u	pore water pressure
v	axial displacement
w_i and w_e	radial displacements of inner and outer specimen wall surfaces, respectively
W	axial load
α_σ	inclination of the major principal stress to the vertical direction
ε_z, ε_r, ε_θ	axial, radial and circumferential normal strains
$\gamma_{z\theta}$	circumferential shear strain
θ	twist deformation

σ	total normal stress
σ'	effective normal stress
σ_z, σ_r, σ_θ	axial, radial and circumferential total normal stresses
σ_1, σ_2, σ_3	major, intermediate and minor total principal stresses
σ_1', σ_2', σ_3'	major, intermediate and minor effective principal stresses
$\tau_{z\theta}$, $\tau_{\theta z}$	circumferential shear stresses

1. Introduction

Geomaterials behave pseudo-elastically up to about 10^{-3} strain. In elastic-plastic modeling, the transition with increasing stress from pseudo-elastic to elastoplastic behavior occurs at the yield point. Hence, the estimation of the yield stress is important in engineering design since it defines the onset of larger plastic deformations with further increases in applied stress. In most ground engineering problems, the principal stresses rotate as the foundation load is applied. For example, Fig. 1 shows the stress conditions at five points (labeled A to E) along a potential rupture surface in the ground. Since most sedimentary deposits are inherently anisotropic, the stiffness and strength responses of the ground foundation will vary from point to point along the rupture surface and are functions of the stress history and both the magnitudes and the directions of the principal stresses. At point D, the major principal stress (σ_1) has rotated through an angle (α_σ) to the vertical direction.

Fig. 1. Stress states along rupture surface.

The hollow cylinder torsional apparatus (HCTA) is uniquely capable of independently controlling the magnitudes of the three principal stresses and the orientation of the major-minor principal stress axes. Hight et al. (1983) and Saada and Townsend (1981) summarized the evolution of HCTA type devices in studying the constitutive response of geomaterials, and in particular sedimentary sand deposits.

This paper describes the use of a state-of-the-art HCTA developed at University College Dublin (UCD) to study the plastic yield behavior of a Leighton Buzzard sand under generalized stress conditions. The development of the apparatus has been reported in detail by O'Kelly and Naughton (2003, 2005a, 2008a). Additional information is presented in this paper on its novel features, in particular the instrumentation, automation and calibration procedures necessary to achieve accurate generalized stress path testing. A series of stress paths were targeted to locate segments of yield loci for the Leighton Buzzard sand in generalized stress space.

The experimental yield data was then compared with the values predicted by two existing yield criteria, namely Matsuoka-Nakai and Lade, in order to assess their accuracy in predicting the onset of plastic yielding in the sand specimens. The two yield criteria are particularly suited to soil mechanics and have been shown by Pradel et al. (1990), Matsuoka et al. (1990) and Lade and Duncan (1976) to provide reasonable predictions for a range of foundation loading conditions. For example, Matsuoka and Nakai (1985) have shown that the Matsuokai-Nakai yield criterion had the effect of averaging the Mohr Coloumb criterion which is widely used in soil mechanics. In contrast, isotropic-kinematic hardening formulations distinguish between primary and secondary yield whereas the bounding surface is allowed to shrink and dilate during cyclic loading in models using bounding surface theory (Pradel et al, 1990). Hence, a direct comparison of the experimental data with isotropic-kinemetic and bounding surface models would have been

difficult to establish and in any event would have had to be examined on a case by case basis.

The Matsuoka-Nakai yield criterion (Matsuoka and Nakai, 1985), which is a theoretical development of the concepts of compoundedly mobilized and spatially mobilized planes, can be expressed in terms of the effective stress invariants, Eq. (1). The Lade yield criterion (Lade and Duncan, 1975), which was developed from analysis of cubical-triaxial test data assuming isotropic behavior, can be best expressed in terms of the first and third effective stress invariants, Eq. (2).

$$\frac{J_1 J_2}{J_3} = \text{Matsuoka-Nakai constant} \tag{1}$$

$$\frac{J_1^3}{J_3} = \text{Lade constant} \tag{2}$$

$$J_1 = \sigma_1' + \sigma_2' + \sigma_3' \tag{3a}$$

$$J_2 = \sigma_1'\sigma_2' + \sigma_2'\sigma_3' + \sigma_3'\sigma_1' \tag{3b}$$

$$J_3 = \sigma_1'\sigma_2'\sigma_3' \tag{3c}$$

where J_1, J_2 and J_3 are the first, second and third effective stress invariants,

and σ_1', σ_2' and σ_3' are the major, intermediate and minor principal effective stresses.

Previous studies, most notably by Pradel et al. (1990), have used HCTA devices to study the effects of a reorientation of the major principal stress on the yield behavior of sand, but only for limited regions of stress space, and with the experimental data reflecting the combined effects of changes in both α_σ and the intermediate principal stress parameter (b):

$$b = \frac{\sigma_2 - \sigma_3}{\sigma_1 - \sigma_3} = \mathrm{Sin}^2\,\alpha_\sigma \qquad (4)$$

The b parameter is a sizing ratio that relates the magnitude of the intermediate principal stress to the magnitudes of the major and minor principal stresses ($0 \leq b \leq 1$). In this paper, the UCD HCTA was used to study the effects of different orientations of the major principal stress and different magnitudes of the b parameter on the yield behavior of the sand separately.

2. Principle of hollow cylinder torsional testing

An axial compressive load (W) and a torque (T) are applied across the length of the thick-walled, hollow-cylindrical test specimen while independently-controlled confining pressures (p_i and p_e) are applied over the inner and outer specimen wall surfaces, Fig. 2(a). The normal stresses acting on an element of the ground foundation are invariably compressive and are simulated in the HCTA by applying the compressive load and confining pressures. Compressive normal stresses are defined as positive in this study. The

test specimen (overall length H and inner and outer radii, r_i and r_e, respectively) may deform axially, radially and twist under the applied surface tractions. A polar coordinate system is appropriate with the z-axis coincident with the specimen axis.

(a) Surface tractions.

(b) Stress components.

(c) Principal stresses.

Fig. 2. Stress state in hollow cylindrical specimen.

Figures 2(b, c) show the non-zero stress components (σ_z, σ_r, σ_θ, $\tau_{z\theta}$) and the resolved principal stresses (σ_1, σ_2, σ_3) that are induced in an element of the specimen wall. The complementary shear stress ($\tau_{\theta z}$) that acts on the vertical plane automatically develops in response to the shear stress $\tau_{z\theta}$ induced by the applied torque. The Lamé equations for calculating the mean values of the non-zero stress components (Table 1) induced across the specimen wall thickness were derived from equilibrium considerations assuming an isotropic, linear-elastic response (Naughton and O'Kelly, 2007). The stress components were integrated over the full specimen volume in order to account for the effects of the specimen wall curvature. From numerical analysis of the test specimen, Wijewickreme (1990) showed that for a given stress component, the difference in the values computed using linear-elastic and more realistic hyperbolic constitutive models were insignificant.

Table 1. Equations for stress and strain components.

Axis direction	Mean stress	Mean strain
Axial normal	$\sigma_z = \frac{W}{\pi(r_e^2 - r_i^2)} + \frac{p_e r_e^2 - p_i r_i^2}{r_e^2 - r_i^2}$	$\varepsilon_z = \frac{v}{H}$
Radial normal	$\sigma_r = \frac{p_e r_e^2 - p_i r_i^2}{r_e^2 - r_i^2} - \frac{2 r_i^2 r_e^2 (p_e - p_i) \ln\left(r_e / r_i\right)}{\left(r_e^2 - r_i^2\right)^2}$	$\varepsilon_r = -\left(\frac{w_e - w_i}{r_e - r_i}\right)$
Circumferential normal	$\sigma_\theta = \frac{p_e r_e^2 - p_i r_i^2}{r_e^2 - r_i^2} + \frac{2 r_i^2 r_e^2 (p_e - p_i) \ln\left(r_e / r_i\right)}{\left(r_e^2 - r_i^2\right)^2}$	$\varepsilon_\theta = -\left(\frac{w_e + w_i}{r_e + r_i}\right)$
Circumferential shear	$\tau_{z\theta} = \frac{4T(r_e^3 - r_i^3)}{3\pi(r_e^4 - r_i^4)(r_e^2 - r_i^2)}$	$\gamma_{z\theta} = \frac{2\theta(r_e^3 - r_i^3)}{3H(r_e^2 - r_i^2)}$

The stress components (σ_z, σ_θ, $\tau_{z\theta}$) are resolved to determine the magnitudes of the major and minor principal stresses and the orientation (α_σ) of the major principal stress to the vertical direction. The intermediate principal stress equals the radial normal stress (σ_r). Hence, the magnitudes of the three principal stresses and the orientation of the major principal stress can be independently controlled by varying the applied surface tractions. The non-zero strain components (ε_z, ε_r, ε_θ, $\gamma_{z\theta}$) are computed from the measured axial (v) and twist (θ) deformations and the radial displacements of the inner and outer specimen wall surfaces, w_i and w_e, respectively (Table 1). Similarly, the strain components are

resolved to determine the magnitudes of the three principal strains and the orientation of the major principal strain to the vertical direction. The HCTA is particularly suited to studying the constitutive behavior of cross-anisotropic test specimens since the major-minor principal stress axes can be rotated relative to the cross-anisotropic plane.

Geomaterials generally comprise three phases, namely: the solid particles; a liquid phase, usually water, and a gaseous phase, usually air (partially saturated conditions). However, the stiffness and strength responses of the test specimen are customarily measured in the fully saturated condition in the geotechnical laboratory, in which case the mechanical response is governed by the effective normal stress (σ') that acts across the contacts between the constituent solid particles. Hence, the stress state must be expressed in terms of the effective stress condition in geotechnical analysis:

$$\sigma' = \sigma - u \qquad \text{(Terzaghi, 1943)} \qquad (5)$$

where σ is the applied or total normal stress;

and u is the pressure in the pore water that fills the saturated voids.

3. UCD hollow cylinder torsional apparatus

3.1. Overview of apparatus

The development of the UCD HCTA (Fig. 3) has been reported in detail by O'Kelly and Naughton (2003, 2005a, 2008a). Additional information on its novel features, particularly the instrumentation, automation and calibration procedures necessary to achieve accurate generalized stress path testing, is presented in this paper.

Fig. 3. UCD hollow cylinder torsional apparatus.

The ends of the test specimen are in contact with annular platens inside an acrylic pressure cell. Hydrostatic confining pressures are applied to the inner and outer specimen wall surfaces using two screw-driven, pressure actuators (each 2.0 MPa and 200 ml in capacity). The inner and outer specimen wall surfaces are enclosed by rubber membranes, typically 0.38-mm in thickness. The outer cell chamber and the specimen inner bore cavity are independently sealed and both chambers are completely filled with water. The rated capacity of the acrylic cylinder limits the confining pressure that can be applied to the outer cell chamber to a maximum of 1.0 MPa. The back pressure applied to the pore water in the specimen and the volume change of the specimen itself (drained test) are controlled by a third pressure actuator.

An axial load and a torque are applied to the bottom end of the specimen via a loading piston that passes thought the base of the cell chamber. The specimen ends are fully

restrained under torsional loading conditions by ribbed, sintered bronze discs that are secured to both the loading and reaction platens. Rotation of the lightly-preloaded screw and spline ball bearings, which were secured to the reaction frame located beneath the pressure cell, can produce smooth vertical, rotary and spiral motions of the loading piston, and hence the loading platen. The top end of the specimen is restrained by a load reaction cage which is located inside the acrylic cylinder in the UCD set up. Under quasi-static loading conditions, the loading mechanisms can apply an axial tension or compression force of up to 19.3 kN and a torque of up to ±103 N.m.

Practical considerations, including the necessary control sensitivity for the applied surface tractions, the strain measurement accuracy and the convenient deployment of instrumentation, particularly in the specimen inner bore cavity, were considered in arriving at the UCD test specimen dimensions of 35.5-mm inner radius, 50.0-mm outer radius and 200-mm in length. Numerical analysis by Naughton and O'Kelly (2007) indicated that the stress non-uniformity that may develop across the thickness of the UCD specimen due to its wall curvature increased in proportion to the major-to-minor principal stress ratio (R), although the level of stress non-uniformity was generally acceptable throughout the stress space for $R \leq 1.5$. The specimen wall thickness of 14.5 mm was also sufficiently large in relation to the grain size of the sand so that a uniform densification of the specimen could be achieved during specimen preparation and potential failure mechanisms were free to develop during the stress path tests.

Based on the capacities of the loading mechanisms and pressure actuators, an axial total normal stress of up to ±5.0 MPa; a radial total normal stress of up to 2.0 MPa and a circumferential shear stress of up to ±0.6 MPa can be induced in the UCD specimen, which is more than adequate to study the stress-strain-strength behavior of geomaterials. Specimens having smaller cross-section areas can be tested by fitting different annular platens in the pressure cell when higher operating stress levels are required.

Stepper-motors drive the mechanisms that actuate the loading piston and pressure actuators to apply small axial and twist boundary displacements and confining pressures to the outer cell chamber and the specimen inner bore cavity. Submersible, high-resolution instrumentation measures the axial load and torque that develop across the specimen length, the applied confining pressures and the axial, radial and twist deformations of the specimen. When the apparatus is operating in precision mode, one step motion by the drive motors displaces or rotates the loading piston by $1x10^{-4}$ mm or 0.8 arc-seconds, corresponding to a control resolution of about $7x10^{-5}$ strain. Errors due to apparatus compliance and specimen end-restraint and bedding effects (Baldi et al., 1988) are excluded by measuring the specimen deformations over a central gauge length using instruments attached or in close proximity to the specimen wall surfaces. The apparatus is located in a temperature-controlled environment at 20 ± 2^{o}C.

3.2. Instrumentation

3.2.1. Applied load, torque and confining pressures

A combined thrust-torque transducer (4.0 kN and 50 N.m in capacity) measures the axial and torsional loads that develop across the specimen length. The transducer is located inside the pressure-cell, next to the restrained end of the specimen, so that measurement errors due to frictional resistance (for example, along the loading piston) do not arise. The thrust-torque transducer was electrically insulated inside a saturated, oil-filled housing that formed part of the reaction platen assembly, Fig. 4.

Fig. 4. Pressure compensation system for thrust-torque transducer.

The transducer readings are unaffected by changes in the confining pressures applied during a test since the confining pressure to the outer cell chamber also acts on the oil contained inside the transducer housing, via a water-oil interface. The transducer was calibrated in-place by applying axial load and torque increments using a system of levers, pulleys and dead weights. The calibration procedure involved the application of an axial load alone, torque alone and combined axial and torsional loading, Fig. 5(a). Typical calibration data for the case of axial loading alone are shown in Fig. 5(b). The coupling between the axial load and torque signals was analyzed using multiple-linear regression which indicated interaction coefficients of typically 1.1%.

Fig. 5. Calibration of thrust-torque transducer.

The two pressure actuators independently control the applied confining pressures to within 0.25 kPa and can target a specified pressure at up to 15 kPa/s. The pressure actuators also measure the volume change of the outer cell chamber and the specimen inner bore cavity. A 400-kPa differential pressure transducer measures the difference in the confining pressures acting across the specimen wall-thickness.

3.2.2. Specimen deformations

The polar deformation response of the test specimen is measured locally using inclinometer gauges and proximity transducers (Figs. 6 and 7) so that the deformation measurements are free from errors associated with apparatus compliance and specimen end-restraint and bedding effects (Baldi et al., 1988). The apparatus is supported entirely on pneumatic mounts which prevent any external vibrations from interfering with the instrument measurements (particularly important at small strain levels).

Fig. 6. Inclinometer gauges: double-axes (left); single-axis (right).

Fig. 7. Specimen set up inside the pressure cell.

The axial and twist specimen deformations are measured over a central 45-mm gauge length using three inclinometer gauges (O'Kelly and Naughton, 2008a,b) that are glued to the outer specimen membrane. Two axial and three twist deformation measurements of up to 20 mm and $\pm 30^{o}$ are measured over the outer specimen wall surface using one single-axis and two double-axes inclinometer gauges, Fig. 6. The radial displacements of the inner and outer wall surfaces are measured near the specimen mid-height using two proximity transducers (O'Kelly and Naughton, 2008c); one transducer is located in the outer cell chamber and the second is located directly opposite in the specimen inner bore cavity. A micro-seal waterproofing treatment was applied to the face of the proximity transducers. Prior to the assembly of the pressure cell, aluminum foil targets are attached by a smear of silicone grease to the rubber membranes that enclose the specimen wall surfaces, preventing any specimen reinforcement effect. Tatsuoka et al. (1983) reported that the displacement of the rubber membranes, and hence the foil targets, matched that of the specimen wall surfaces. Each foil target is made large enough to accommodate the anticipated relative movements between the proximity transducers and the specimen wall surfaces during the course of a test.

The inclinometer gauges and proximity transducers were calibrated using an optical table that allowed set displacements to a resolution of 0.0025 mm in three orthogonal directions. The calibration procedure for the inclinometer gauges, which were found to have a linear response for tilt angles of up to 10^{o}, has been reported by O'Kelly and Naughton (2008a,b).

The proximity transducers were calibrated while fully submerged under water since the transducer response is sensitive to its operating environment. The gap between the transducer face and the targets (two plastic discs covered with aluminum foil that had the same curvatures as the inner and outer specimen wall surfaces) were measured using a laser distance-measurement system that had resolution and accuracy values of the order of 10^{-12} and 10^{-11} m, respectively. The data curves for calibration in air and fully submerged in water were found to differ by between 0.07 and 0.09 mm over the measurement range of 0.5 to 5.0 mm. The local instrumentation had a measurement range of between 10^{-5} and 10^{-1} strain (i.e. pseudo-elastic to failure strain levels for geomaterials), covering the full strain range of engineering interest. Existing HCTA devices have had to incorporate dynamic measurement techniques, including shear wave velocity and resonant column tests (Connolly and Kuwano, 1999; Drnevich, 1985), in order to extend the strain measurement capability into the pseudo-elastic range. The output signals from the different instruments were recorded at 5 min intervals over the 24 hour period proceeding each stress path test and the electrical stability of the outputs was found to be satisfactory (standard deviation from the mean output voltage was generally significantly less than 0.5%). Longer-term checks were periodically carried out and again the stability of the outputs was found to be satisfactory.

3.2.3. Automatic stress path control

Figure 8 shows a schematic of the data acquisition and control systems for the UCD HCTA. The drive units and the pressure actuators interface with a personal computer via Compumotor® interconnect cards and a general-purpose interface bus. The apparatus was closed-loop controlled to target a user-defined stress path using a suite of LabVIEW® programs, Fig. 9.

Fig. 8. Schematic of data acquisition and control systems.

Fig. 9. Flow chart for control algorithms.

Firstly, the prescribed stress path is read from a data file. The load, pressure and deformation instruments are simultaneously scanned to determine their initial reference outputs. The target values of the surface tractions are computed from the mean effective stress components that correspond to a series of transition stress points located along the stress path. The loading mechanisms and pressure actuators apply small axial and twist displacements and confining pressures to the specimen surfaces by independently controlling the direction and step rate of the motor drives. The axial load and torque that are induced across the specimen length are controlled by the thrust-torque transducer in a feedback loop. The instruments are continuously scanned and their outputs and initial reference values compared to determine the actual values of the applied surface tractions

and the specimen deformations. The actual state of effective stress and the strain response are computed in real time using the equations in Table 1. The two axial and three twist deformations measured by the inclinometer gauges are used to compute the specimen axial normal and circumferential shear strain values, respectively. The radial displacements of the specimen wall surfaces recorded by the proximity transducers are used to calculate the radial and circumferential normal strain values. The stress path is followed by sequentially stepping between transition target stress-points located along the prescribed stress path.

The stiffness and strength of sand and gravel deposits (frictional materials) are directly related to the major-to-minor effective principal stress ratio, R'. Hence, it is preferable to express the stress path in terms of an alternative but equivalent set of control parameters, namely: the mean effective confining stress (p'); b parameter; R' and α_σ (Table 2).

Table 2. Control parameters used in the algorithms.

Stress parameter	Equation	Max difference between target stress points
Mean effective confining stress	$p' = \frac{\sigma'_1 + \sigma'_2 + \sigma'_3}{3}$	5.0 kPa

Intermediate principal stress parameter	$b = \frac{\sigma'_2 - \sigma'_3}{\sigma'_1 - \sigma'_3}$	0.1
Major-to-minor effective principal stress ratio	$R' = \frac{\sigma'_1}{\sigma'_3}$	0.1
Major-to-minor principal stress difference	$t = \sigma'_1 - \sigma'_3$	5.0 kPa
Angle of major principal stress to vertical direction	$\alpha_\sigma = \frac{1}{2}\mathrm{Tan}^{-1}\left(\frac{2\tau_{z\theta}}{\sigma'_z - \sigma'_\theta}\right)$	5.0 degree

The key change points along the stress path, as well as the transition target stress points, are expressed in terms of the set of control parameters. The control algorithm loops and the loading mechanisms and pressure actuators are simultaneously adjusted to bring all of the effective stress components within specified tolerances for the target values (default set at 0.25 kPa). The algorithm considers the impact that a change in the value of one control parameter would have on the other parameters in determining step size taken by the drive motors. The specimen deformations are allowed to equilibrate at each target point along the stress path. Equilibrium is deemed to have been achieved when the rate of change in the strain components are all within the limits specified in Table 3. The equilibrium check is bypassed if the specimen has not achieved equilibrium within a specified number of loops through the control algorithm in which case the specimen is assumed to be approaching the onset of shear failure and the applied surface tractions are readjusted in order to follow the

prescribed stress path as closely as possible. The control algorithm includes calibration equations for the different instruments and automatically corrects the specimen stresses for the restraining effects of the rubber membranes that enclose the outer and inner specimen wall surfaces (Sivathayalan and Vaid, 1998; Tatsuoka et al., 1986).

Table 3. Limiting rates that identify whether the specimen has achieved equilibrium.

Stress component	Unit	Rate
Axial, radial and circumferential normal strains	strain/min	$5x10^{-5}$
Circumferential shear strain		$1x10^{-5}$
Pore water pressure	kPa/min	0.5

4. Study of the plastic yield behavior of sand

4.1. Overview

The UCD HCTA was used to study the plastic yield behavior of a Leighton Buzzard sand under generalized stress conditions, and in particular the effects of a reorientation of the major principal stress and changes in the magnitude of the b parameter. The stress paths systematically probed generalized stress space using the methodology of Tatsuoka and Ishihara (1974) in order to locate a series of yield points that allowed segments of

developing yield loci to be identified for the sand. After isotropically consolidating the test specimens to the same mean effective confining stress, new fabrics were induced in the specimens by following prescribed anisotropic consolidation stages that targeted different α_σ values, and with the intermediate principal stress parameter b = 0 or 0.5. Yield points were then identified for prescribed b parameter values in the range $0 \leq b \leq 1.0$ by increasing the R' value until plastic straining commenced. This systematic approach allowed the effects of the reorientation of the major principal stress and the changes in the magnitude of the b parameter to be independently studied. The accuracy of the Matsuoka-Nakai and Lade yield criteria (Eqs. (1) and (2)) in predicting the onset of plastic yielding in the sand specimens was assessed by comparing the predicted and experimental yield values.

4.2. Materials and specimen preparation method

The test material was a white, clean, fine-to-medium Leighton Buzzard sand that comprised sub-angular grains, about 0.5-mm in size (Table 4). The sand in its loosest state had a maximum void ratio (defined as the volume of the void space to the volume of the sand grains) of 0.80. In its densest state, the sand had a minimum void ratio of 0.53. Eight, physically identical test-specimens were prepared using a water-pluviation technique (O'Kelly and Naughton, 2005b), which mimicked the sedimentation process, producing specimens with an inherent cross-anisotropic fabric similar to that of many natural sand deposits. Inner and outer cylindrical moulds that had been lined with rubber membranes

were set up on the specimen loading platen. The test specimens were prepared to an initial target void ratio of 0.73 by slowly depositing the saturated sand into the annular, water-filled cavity between the cylindrical moulds. The eight test specimens were densified to a medium dense state (target void ratio of 0.60) by uniformly tapping around the outer mould using a mallet. The local instrumentation was set up after removing the preparation moulds. Next, the pressure cell was fitted and secured to the support frame. The outer cell chamber and the specimen inner bore cavity were simultaneously flooded with water and pressurizing to 150 kPa, and with a backpressure of 100 kPa applied to the specimen (p' = 50 kPa). Full saturation of the sand was achieved in this manner.

Table 4. Physical properties of Leighton Buzzard sand.

Coefficient of uniformity, C_U	1.32
Coefficient of curvature, C_Z	0.96
Effective grain size, D_{10} (mm)	0.44
Specific gravity of solids	2.64
Maximum void ratio	0.80
Minimum void ratio	0.53

4.3. Experimental methodology

The stress path tests comprised four stages, as follows, with Fig. 10 showing a characteristic stress path plotted in terms of R' versus the b parameter:

Stage 1: The inner and outer confining pressures were simultaneously increased from 150 to 200 kPa and the specimen was allowed to drain overnight against the applied specimen back pressure which was continuously adjusted in order to maintain the mean effective confining stress p' = 100 kPa (point A).

Stage 2: Next the specimen was consolidated anisotropically by increasing the effective principal stress ratio R' from 1.0 to 1.5 and re-orientating the major principal stress to an angle of α_σ = 0, 30, 60 or 90 degrees from the vertical direction, which induced a in the specimens. During this stage, the b parameter value was either maintained constant at b = 0 or increased from b = 0 to 0.5. The values of p' and α_σ were then held constant along the remaining stages of the stress path.

Stage 3: A yield point (point B) was established by increasing the R' value until plastic straining of the specimen commenced, which was characterized by a marked change in its stiffness response. An initial yield point was established at R' = 2.1 for the eight specimens tested in this study.

Stage 4: After establishing a yield point, the R' value was reduced (point C) and the specimen was reconsolidated to increase the b parameter value by 0.25 (point D).

With the b parameter value set, the R' value was increased again to search for a second yield point (point E). This allowed a yield locus to be established between points B and E. The procedure was repeated to establish segments of yield loci for different stress states in the specimens.

Fig. 10. Stress probing to identify yield loci.

The test program identified 16 segments of yield loci distributed throughout the stress space. Care was taken to limit the development of plastic straining during the reconsolidation stages of the stress paths. Significant plastic straining would have increased the transition zone between pseudo-elastic and post-yield behavior making it more difficult to accurately define the yield point value.

4.4. Experimental results and analysis

The eight test-specimens had been prepared to similar initial void ratio values of between 0.59 and 0.61 using a wet-pluviation technique, and hence had similar cross-anisotropic fabrics initially. Naughton and O'Kelly (2003) have shown experimentally that the stress-strain response of the Leighton Buzzard sand was not significantly affected by this level of variation in the initial void ratio under isotropic loading conditions.

A typical data set, including the actual and target stress paths and the measured strain responses, is shown in Fig. 11 for the case of p' = 100 kPa, $\alpha_\sigma = 30^o$, and with the b parameter value being increased in 0.25 steps from b = 0.5 at the end of the anisotropic consolidation stage 2 to b = 1.0 by the end of the stress path test. The prescribed stress path is defined by the continuous line segments in Fig. 11(a). The key change points on the stress path and the corresponding strain values are also labeled alphabetically, namely points A to K. Figure 11(b) shows the manner in which the four stress components (σ_z', σ_r', σ_θ', $\tau_{z\theta}$) were continuously adjusted by the control program in order to follow the prescribed stress path to within 2% of the target values. Figures 11(c, d) show the strain responses recorded during the load-unload and reconsolidation stages of the stress path (i.e. changes in the R' and b parameter values, respectively). The stress-strain responses in Fig. 11(c) were approximately linear-elastic along the unload paths and along the initial phase of the reload paths. Furthermore, the strains during the reconsolidation stages were negligible. Hence, the soil fabric induced in the specimens by the end of the anisotropic consolidation stage 2 would have remained largely intact for the remainder of the stress path.

Fig. 11. Stress probing to determine yield points.

However, the stress-strain responses became increasingly non-linear on nearing a yield point. Pradel et al. (1990) suggested that the yield points derived from the intersection of the best-fit lines to the initial pseudo-elastic and post-yield slopes provided the most appropriate estimate of the yield loci for the Matsuokai-Nakai and Lade yield criteria. Hence, the yield point was identified by curve-fitting the experimental plots. A segment of the yield locus was defined by joining the yield point established for higher values of the b parameter back to the initial yield point. Minor discrepancies arose in the experimental values determined for a specific yield point identified by curve-fitting analysis of the different stress-strain responses (coefficient of variation in the R' value of between 0.2% and 10.9%). Similar differences were also reported in the experimental study by Pradel et al. (1990). Hence, the stress state corresponding to a specific yield point in this study was calculated as the mean value from curve-fitting analysis of a minimum of four experimental stress-strain curves.

Figure 12 shows the experimental yield data plotted in terms of α_σ, the b parameter and the deviator stress (q), given by:

$$q = \sqrt{\left(\sigma_1^{'} - \sigma_3^{'}\right)^2 + \left(\sigma_1^{'} - \sigma_2^{'}\right)^2 + \left(\sigma_2^{'} - \sigma_3^{'}\right)^2} \quad (6)$$

Fig. 12. Variation of deviator stress on yield loci.

The experimental data suggests that the magnitude of the deviator stress corresponding to the yield loci varies continuously, although in a well-defined pattern, namely: the deviator stress at yield was dependent on the initial value of the b parameter but was largely independent of the α_σ rotation that had occurred during the anisotropic consolidation stage of the stress path. It is plausible that the densification of the specimens by tapping around the cylindrical moulds during specimen preparation had significantly reduced the initial level of cross-anisotropy that had been created by the wet-pluviation technique. Two trends are observed with respect to the b parameter, namely:

(i) Stress paths that had re-orientated the major principal stress, and with the intermediate principal stress parameter value initially set at b = 0: the deviator stress at yield decreased by typically 15% to 20% due to the increase in the b parameter value from b = 0 to 0.5;

(ii) Stress paths that had re-orientated the major principal stress, and with the b parameter value initially set at 0.5: the magnitude of the deviator stress at yield either remained constant or increased marginally due to the increase in the b parameter value from to b = 0.5 to 1.0.

The experimental yield loci are compared with the predictions given by the Matsuoka-Nakai and Lade yield criteria in Fig. 13. The experimental data are expressed in terms of

the respective yield constants (Eqs. (1) and (2)), and normalized to allow direct comparisons with the theoretical values predicted by the two yield criteria.

(a) Matsuoka-Nakai criterion.

(b) Lade criterion.

Fig. 13. Experimental and theoretical values of points on yield loci.

The two yield criteria were found to slightly underestimate the onset of yielding for $0 \leq b \leq 0.5$ and slightly overestimate the onset of yielding for $0.5 < b \leq 1.0$. However, given the approximate nature of the curve-fitting analysis that had been used in determining the experimental yield values, it is concluded that both yield criteria provide satisfactory predictions of the onset of plastic yielding in sand under generalized stress conditions. The margin of error in the experimental yield loci from the curve-fitting analysis (coefficient of variation in the R' value of between 0.2% and 10.9%) prohibits the identification of the specific mechanism(s) that give rise to the minor discrepancies with the two yield criteria studied since several mechanisms may be simultaneously mobilized. The experimental yield loci may also resemble inflated balloons in principal stress space rather than the conical shapes with smooth triangular cross-sections given by the theoretical models. However, it is concluded that both yield criteria adequately account for changes in the

intermediate principal stress parameter in the prediction of the onset of plastic yielding in sand deposits for routine geotechnical engineering design.

5. Summary and conclusions

A versatile hollow cylinder torsional apparatus (HCTA) was used to systematically probe generalized stress space in order to locate segments of yield loci for a fully saturated Leighton Buzzard sand. Eight, physically identical test-specimens (35.5-mm inner radius, 50.0-mm outer radius and 200-mm in length) were prepared using a water-pluviation technique that mimicked the sedimentation process, and hence the inherent cross-anisotropic fabric of many natural sand deposits. The stresses induced in the test specimens were continually adjusted to within 2% of the target values on the prescribed stress paths, which comprised in sequence: an isotropic consolidation stage to the same mean effective confining stress; an anisotropic consolidation stage that produced different reorientations of the major principal stress and finally probing of the stress space to locate segments of developing yield loci. The specimen deformation response was measured to a resolution of 10^{-5} strain over its central gauge length. Novel features of the HCTA, particularly the instrumentation, automation and calibration procedures that were necessary to achieve accurate generalized stress path testing, are presented.

The deviator stress at yield for the saturated Leighton Buzzard sand was found to vary in a well-defined pattern in the stress space, namely: the deviator stress at yield was dependent

on the initial value of the intermediate principal stress parameter but was largely independent of the stress reorientation that occurred during the anisotropic consolidation stage of the stress path. The Matsuoka-Nakai and Lade yield criteria were both found to provide satisfactory predictions of the onset of plastic yielding in the sand under generalized stress conditions for routine geotechnical engineering design.

Acknowledgements

The authors would like to acknowledge the support of Dr. Tom Widdis and Professor Eugene O'Brien during the course of the research, which was carried out at the Department of Civil Engineering, University College Dublin (UCD). The paper was written by the lead author while on sabbatical leave at the Urban Institute Ireland, UCD. The lead author is also grateful for funding received through the Pierse-Newman Scholarship in Civil Engineering from UCD.

References

Baldi, G., Hight, D.W., Thomas, G.E., 1988. A reevaluation of conventional triaxial test methods. In: Advanced Triaxial Testing of Soils and Rock, ASTM STP977, Philadelphia.

Connolly, T.M., Kuwano, R., 1999. The measurement of G_{max} in a resonant column, bender elements, torsional shear apparatus. In: Proceedings Second International Symposium on Pre-failure Deformation Characteristics of Geomaterials, Torino, Italy, 1, 73–80.

Drnevich, V.P., 1985. Recent developments in resonant column testing. In: Proceedings Richart Commemorative Lectures, ASTM Specialty Session, Detroit, pp. 79–107.

Hight, D.W., Gens, A., Symes, M.J., 1983. The development of a new hollow cylinder apparatus for investigating the effects of principal stress rotation in soils. Géotechnique 33(4), 355–383.

Lade, P.V., Duncan, J.M., 1975. Elastoplastic stress strain theory for cohesionless soil. ASCE Geotechnical Engineering J. 101(GT10), 1037–1053.

Matsuoka, H., Nakai, T., 1985. Relationship among Tresca, Mises, Mohr-Coulomb and Matsuoka-Nakai failure criteria. Soils and Foundations 25(4),123–128.

Matsuoka, H., Suzuki, Y., Murata, T., 1990. A constitutive model for soils evaluating principal stress rotation and its application to some deformation problems. Soils and Foundations 30(1), 142–154.

Naughton, P.J., O'Kelly, B.C., 2003. The anisotropy of Leighton Buzzard sand under general stress conditions. In: Proceedings Third International Symposium on Deformation Characteristics of Geomaterials, Lyon, France, 1, 285–291.

Naughton, P.J., O'Kelly, B.C., 2007. Stress non-uniformity in a hollow cylinder torsional sand specimen. Geomechanics and Geoengineering 2(2), 117–122.

O'Kelly, B.C., Naughton, P.J., 2003. Development of the University College Dublin hollow cylinder apparatus. In: Proceedings 56th Canadian Geotechnical Conference, Winnipeg, Ontario.

O'Kelly, B.C., Naughton, P.J., 2005a. Development of a new hollow cylinder apparatus for stress path measurements over a wide strain range. ASTM Geotechnical Testing J. 28(4), 345–354.

O'Kelly, B.C., Naughton, P.J., 2005b. Engineering properties of wet-pluviated hollow cylindrical specimens. ASTM Geotechnical Testing J. 28(6), 570–576.

O'Kelly B.C.; Naughton P.J., 2008a. Local measurements of the polar deformation response in a hollow cylinder apparatus, Geomechanics and Geoengineering (in press).

O'Kelly B.C.; Naughton P.J., 2008b. Measuring shear strain in a hollow cylinder apparatus using electrolevel-inclinometer gages. In: Proceedings Fourth International Symposium on Pre-Failure Deformation Characteristics of Geomaterials, Atlanta, Georgia, USA.

O'Kelly B.C.; Naughton P.J., 2008c. Use of proximity transducers for local radial strain measurements in a hollow cylinder apparatus. In: Proceedings Fourth International Symposium on Pre-Failure Deformation Characteristics of Geomaterials, Atlanta, Georgia, USA.

Pradel, D., Ishihara, K., Gutierrez, M., 1990. Yielding and flow of sand under principal stress axes rotation. Soils and Foundations 30(1), 87–99.

Saada, A.S., Townsend, F.C., 1981. State of the art: laboratory strength testing of soils. In: Laboratory Shear Strength of Soils, ASTM STP740, Philadelphia, pp. 7–77.

Sivathayalan, S., Vaid, Y.P., 1998. Truly undrained response of granular soils with no membrane penetration effects. Canadian Geotechnical J. 35, 730–739.

Tatsuoka, F., Ishihara, K., 1974. Yielding of sand in triaxial compression. Soils and Foundations 14(2), 63–76.

Tatsuoka, F., Muramatsu, M., Saski, T., 1983. *Closure to* Cyclic undrained stress-strain behavior of dense sands by torsional simple shear tests. Soils and Foundations 23(3), 142–145.

Tatsuoka, F., Sonoda, M., Hara, K., Fukushima, S., Pradhan, T.B.S., 1986. Failure and deformation of sand in torsional shear. Soils and Foundations 26(4), 79–97.

Terzaghi, K., 1943. Theoretical Soil Mechanics. John Wiley and Sons, New York.

Wijewickreme, D., 1990. Behavior of sand under simultaneous increase in stress ratio and rotation of principal stresses. PhD thesis, University of British Colombia, Canada.

Figure captions

Fig. 1. Stress states along rupture surface.

(a) Surface tractions.

(b) Stress components.

(c) Principal stresses.

Fig. 2. Stress state in hollow cylinder torsional specimen.

Fig. 3. UCD hollow cylinder torsional apparatus.

Fig. 4. Pressure compensation system for thrust-torque transducer.

(a) Loading sequences.

(b) Axial load calibration data.

Fig. 5. Calibration of thrust-torque transducer.

Fig. 6. Inclinometer gauges: double-axes (left); single-axis (right).

Fig. 7. Specimen set up inside the pressure cell.

Fig. 8. Schematic of data acquisition and control systems.

Fig. 9. Flow chart for control algorithms.

Fig. 10. Stress probing to identify yield loci.

Fig. 11. Stress probing to determine yield points.

Fig. 12. Variation of deviator stress on yield loci.

(a) Matsuoka-Nakai criterion.

(b) Lade criterion.

Fig. 13. Experimental and theoretical values of points on yield loci.

Table captions

Table 1. Equations for stress and strain components.

Table 2. Control parameters used in the algorithms.

Table 3. Limiting rates that identify whether the specimen has achieved equilibrium.

Table 4. Physical properties of Leighton Buzzard sand.

Study of the yielding of sand under generalized stress conditions using a versatile hollow cylinder torsional apparatus

Brendan C. O'Kelly and Patrick J. Naughton

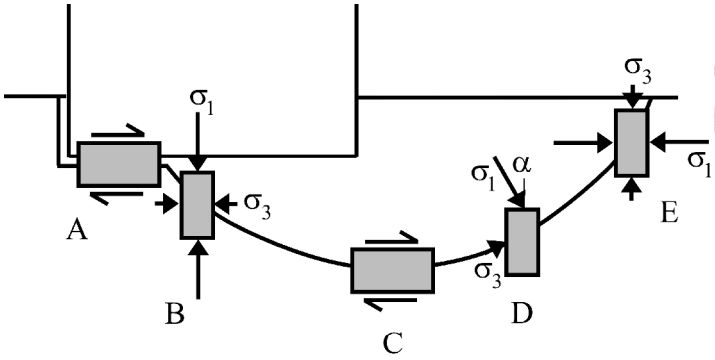

Fig. 1. Stress states along rupture surface.

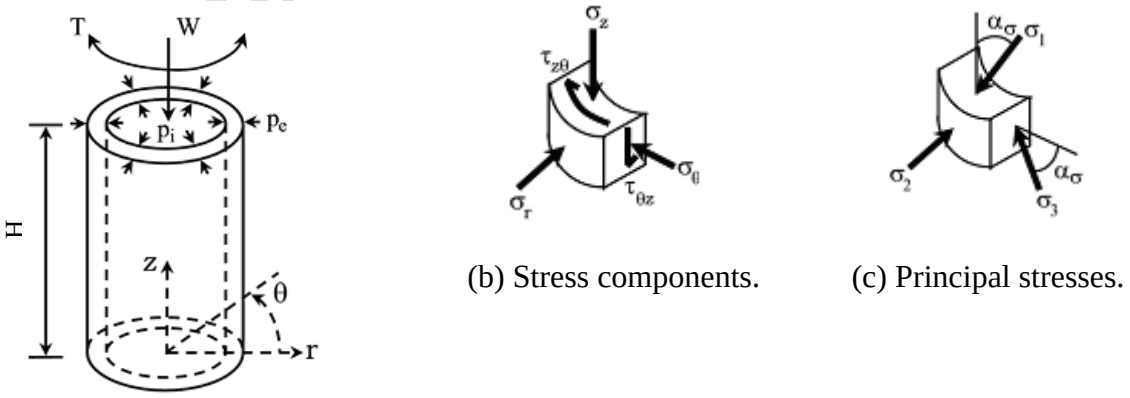

(a) Surface tractions.

(b) Stress components.

(c) Principal stresses.

Fig. 2. Stress state in hollow cylinder torsional specimen.

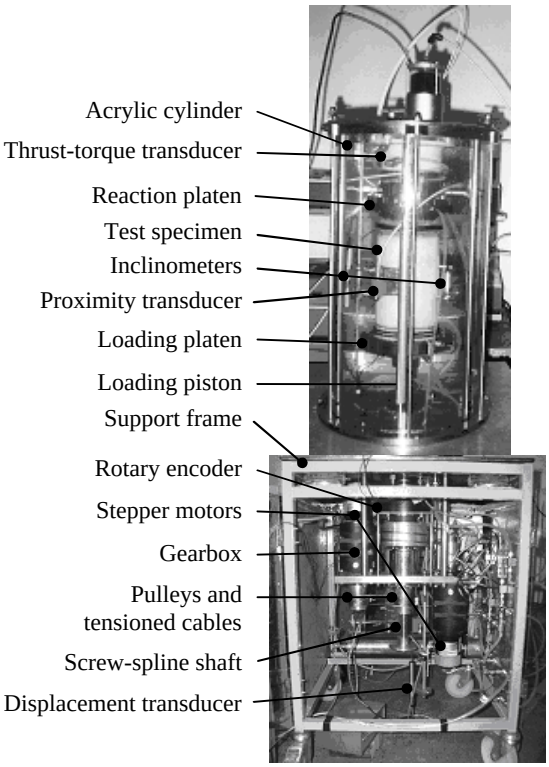

Fig. 3. UCD hollow cylinder torsional apparatus.

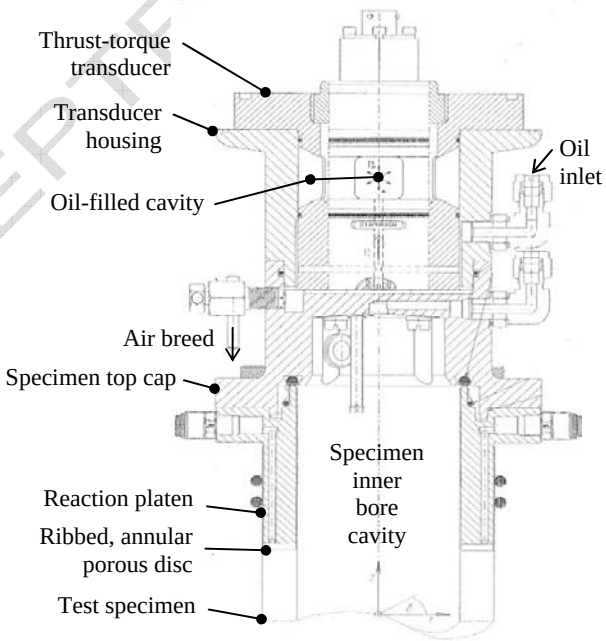

Fig. 4. Pressure compensation system for thrust-torque transducer.

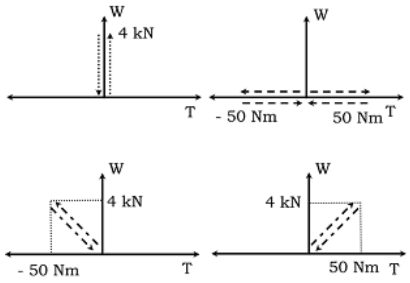

(a) Loading sequences.

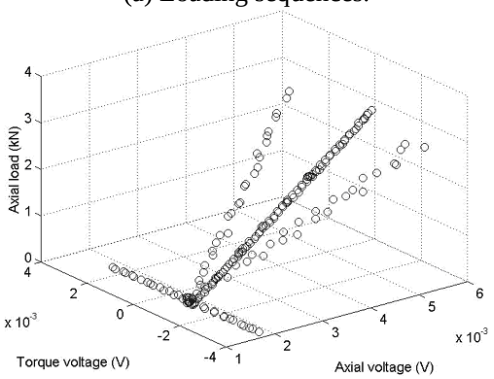

(b) Axial load calibration data.

Fig. 5. Calibration of thrust-torque transducer.

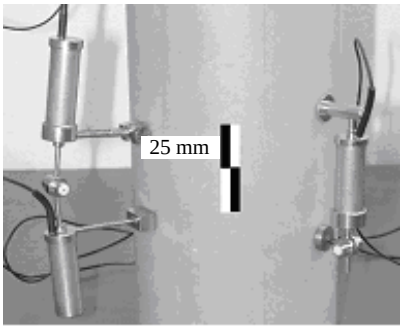

Fig. 6. Inclinometer gauges: double-axes (left); single-axis (right).

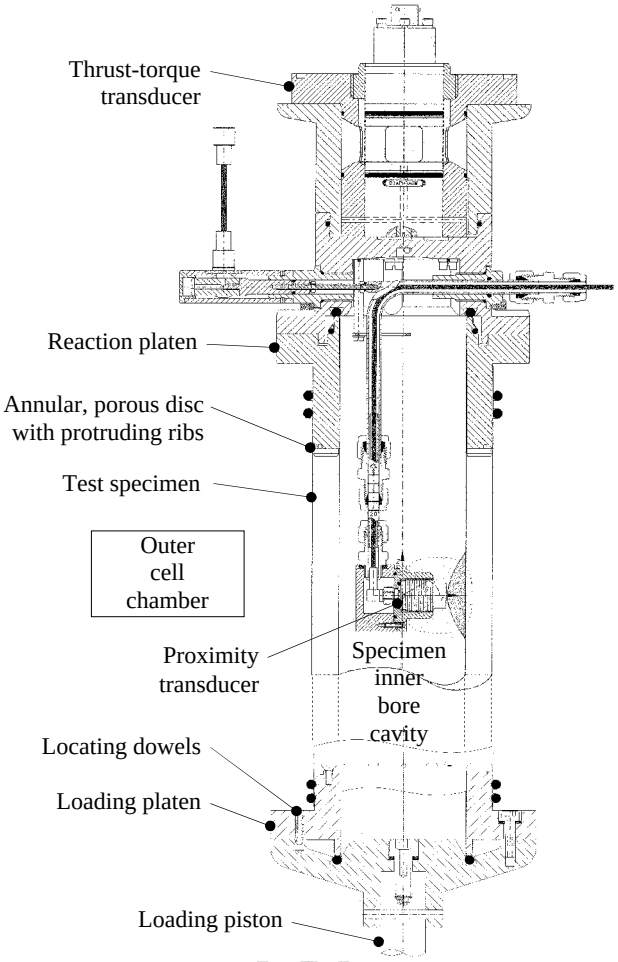

Fig. 7. Specimen set up inside the pressure cell.

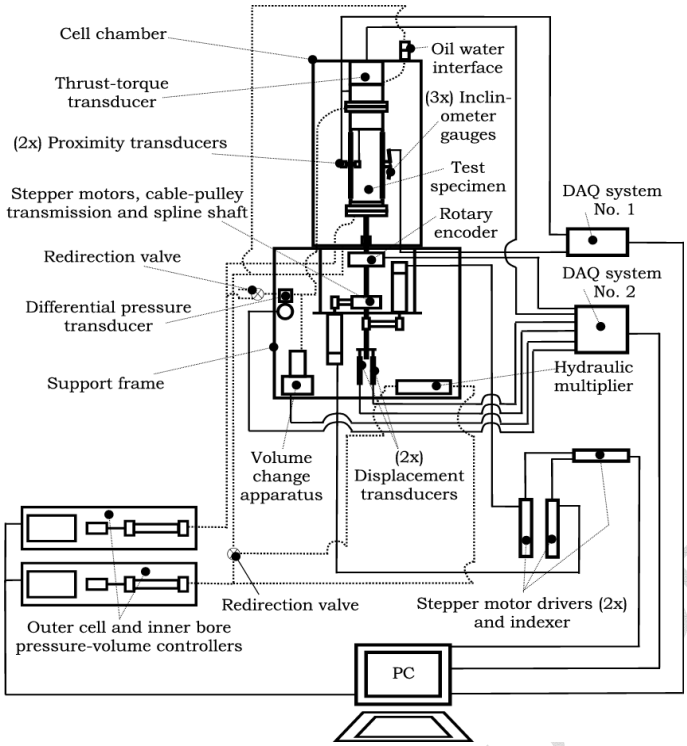

Fig. 8. Schematic of data acquisition and control systems.

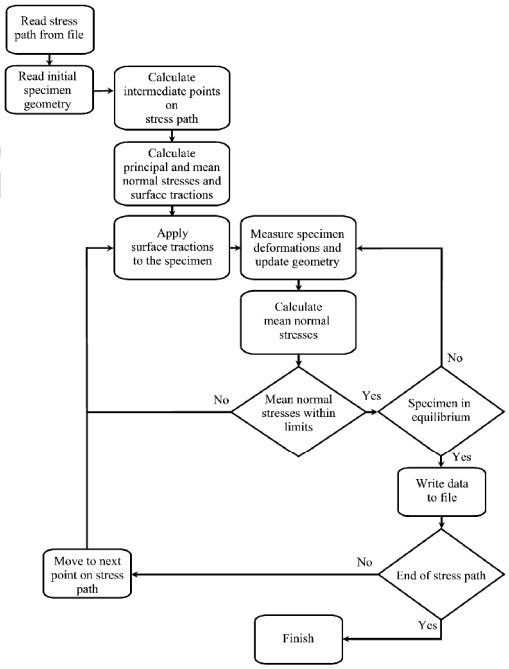

Fig. 9. Flow chart for control algorithms.

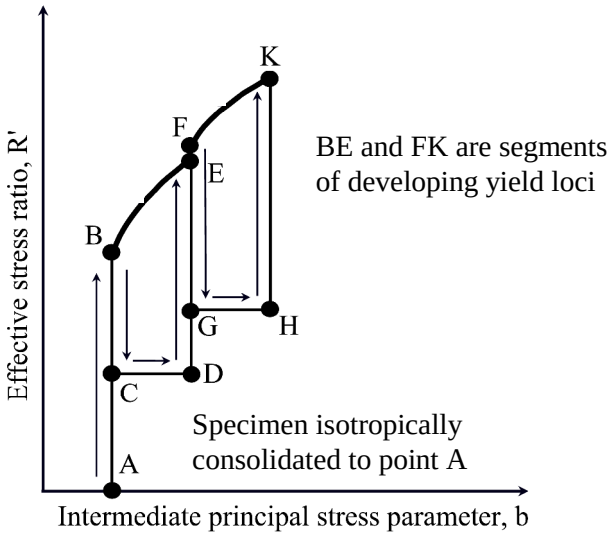

Fig. 10. Stress probing to identify yield loci.

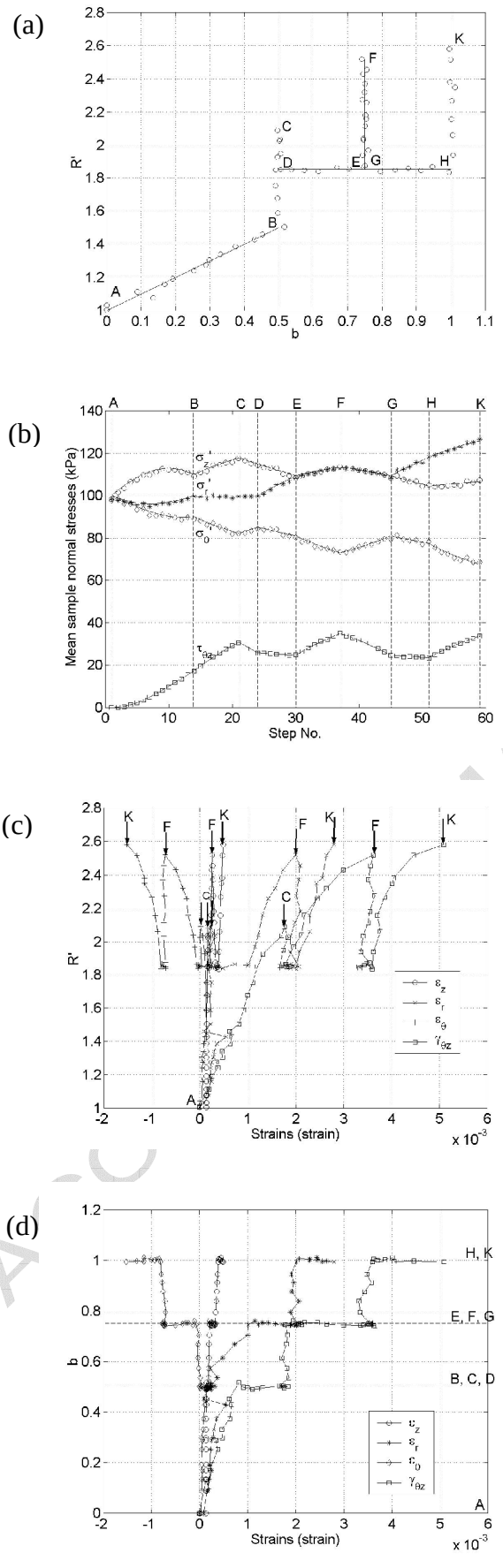

Fig. 11. Stress probing to determine yield points.

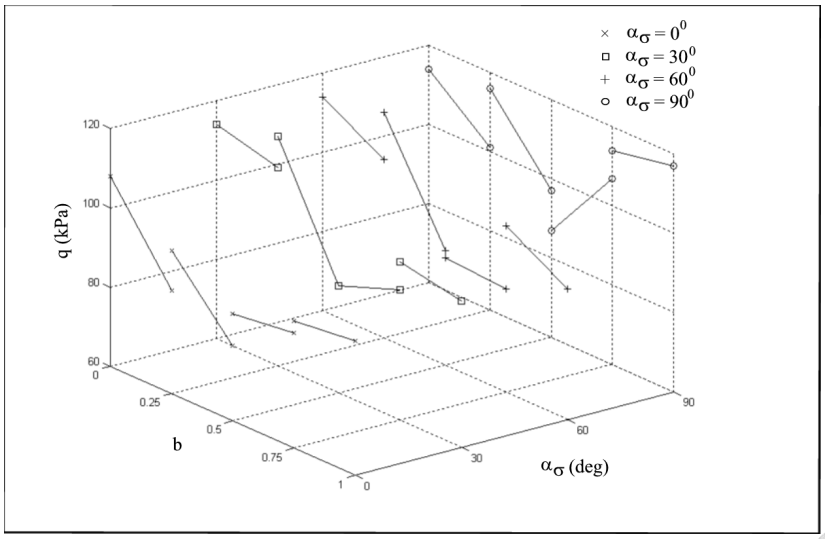

Fig. 12. Variation of deviator stress on yield loci.

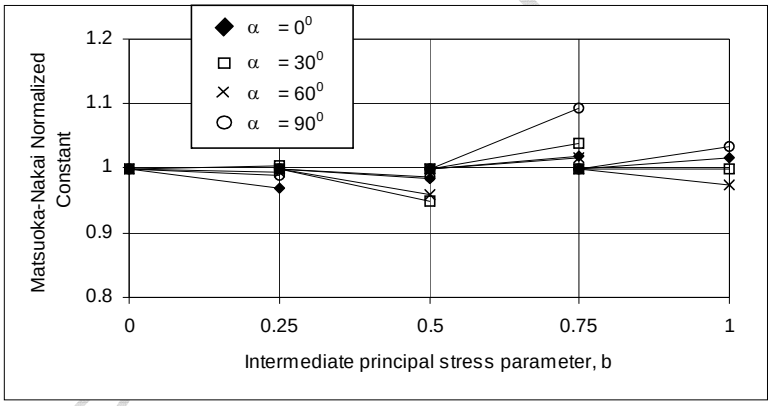

(a) Matsuoka-Nakai criterion.

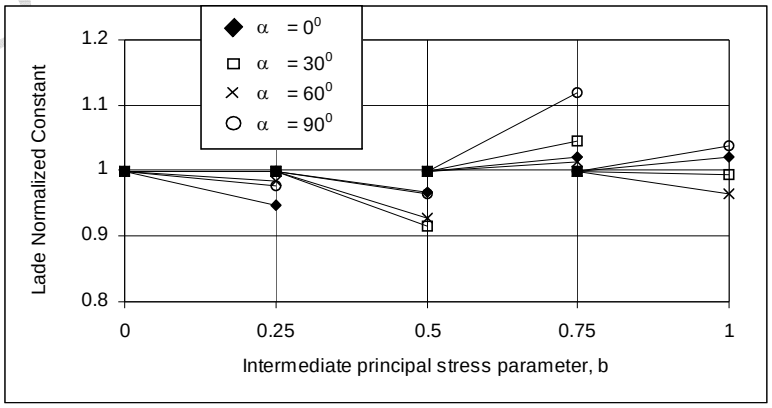

(b) Lade criterion.

Fig. 13. Experimental and theoretical values of points on yield loci.

Study of the yielding of sand under generalized stress conditions using a versatile hollow cylinder torsional apparatus

Brendan C. O'Kelly and Patrick J. Naughton

Table 1. Equations for stress and strain components.

Axis direction	Mean stress	Mean strain
Axial normal	$\sigma_z = \frac{W}{\pi(r_e^2 - r_i^2)} + \frac{p_e r_e^2 - p_i r_i^2}{r_e^2 - r_i^2}$	$\varepsilon_z = \frac{v}{H}$
Radial normal	$\sigma_r = \frac{p_e r_e^2 - p_i r_i^2}{r_e^2 - r_i^2} - \frac{2 r_i^2 r_e^2 (p_e - p_i) \ln\left(r_e / r_i\right)}{\left(r_e^2 - r_i^2\right)^2}$	$\varepsilon_r = -\left(\frac{w_e - w_i}{r_e - r_i}\right)$
Circumferential normal	$\sigma_\theta = \frac{p_e r_e^2 - p_i r_i^2}{r_e^2 - r_i^2} + \frac{2 r_i^2 r_e^2 (p_e - p_i) \ln\left(r_e / r_i\right)}{\left(r_e^2 - r_i^2\right)^2}$	$\varepsilon_\theta = -\left(\frac{w_e + w_i}{r_e + r_i}\right)$
Circumferential shear	$\tau_{z\theta} = \frac{4T(r_e^3 - r_i^3)}{3\pi(r_e^4 - r_i^4)(r_e^2 - r_i^2)}$	$\gamma_{z\theta} = \frac{2\theta(r_e^3 - r_i^3)}{3H(r_e^2 - r_i^2)}$

Table 2. Control parameters used in the algorithms.

Stress parameter	Equation	Max difference between target stress points
Mean effective confining stress	$p' = \frac{\sigma'_1 + \sigma'_2 + \sigma'_3}{3}$	5.0 kPa
Intermediate principal stress parameter	$b = \frac{\sigma'_2 - \sigma'_3}{\sigma'_1 - \sigma'_3}$	0.1
Major-to-minor effective principal stress ratio	$R' = \frac{\sigma'_1}{\sigma'_3}$	0.1
Major-to-minor principal stress difference	$t = \sigma'_1 - \sigma'_3$	5.0 kPa
Angle of major principal stress to vertical direction	$\alpha_\sigma = \frac{1}{2}\mathrm{Tan}^{-1}\left(\frac{2\tau_{z\theta}}{\sigma'_z - \sigma'_\theta}\right)$	5.0 degree

Table 3. Limiting rates that identify whether the specimen has achieved equilibrium.

Stress component	Unit	Rate
Axial, radial and circumferential normal strains	strain/min	$5x10^{-5}$
Circumferential shear strain		$1x10^{-5}$
Pore water pressure	kPa/min	0.5

Table 4. Physical properties of Leighton Buzzard sand.

Coefficient of uniformity, C_U	1.32
Coefficient of curvature, C_Z	0.96
Effective grain size, D_{10} (mm)	0.44
Specific gravity of solids	2.64
Maximum void ratio	0.80
Minimum void ratio	0.53